The Astrophysical Journal, 677:657–670, 2008 April 10

XO-3b: A MASSIVE PLANET IN AN ECCENTRIC ORBIT TRANSITING AN F5 V STAR

Christopher M. Johns-Krull,[1,2] Peter R. McCullough,[3] Christopher J. Burke,[3] Jeff A. Valenti,[3]
K. A. Janes,[4] J. N. Heasley,[5] L. Prato,[6] R. Bissinger,[7] M. Fleenor,[8] C. N. Foote,[9]
E. Garcia-Melendo,[10] B. L. Gary,[11] P. J. Howell,[4]
F. Mallia,[12] G. Masi,[13] and T. Vanmunster[14]

Received 2007 September 17; accepted 2007 December 20

ABSTRACT

We report the discovery of a massive planet ($M_p \sin i = 13.02 \pm 0.64\ M_J$; total mass = $13.25 \pm 0.64\ M_J$), large ($1.95 \pm 0.16\ R_J$) planet in a transiting, eccentric orbit ($e = 0.260 \pm 0.017$) around a 10th magnitude F5 V star in the constellation Camelopardalis. We designate the planet XO-3b and the star XO-3, also known as GSC 03727−01064. The orbital period of XO-3b is 3.1915426 ± 0.00014 days. XO-3 lacks a trigonometric parallax; we estimate its distance to be 260 ± 23 pc. The radius of XO-3 is $2.13 \pm 0.21\ R_\odot$, its mass is $1.41 \pm 0.08\ M_\odot$, its $v \sin i = 18.54 \pm 0.17$ km s^{-1}, and its metallicity is $[\mathrm{Fe/H}] = -0.177 \pm 0.027$. This system is unusual for a number of reasons. XO-3b is one of the most massive planets discovered around any star for which the orbital period is less than 10 days. The mass is near the deuterium-burning limit of $13\ M_J$, which is a proposed boundary between planets and brown dwarfs. Although Burrows et al. propose that formation in a disk or formation in the interstellar medium in a manner similar to stars is a more logical way to differentiate planets and brown dwarfs, our current observations are not adequate to address this distinction. XO-3b is also unusual in that its eccentricity is large given its relatively short orbital period. Both the planetary radius and the inclination are functions of the spectroscopically determined stellar radius. Analysis of the transit light curve of XO-3b suggests that the spectroscopically derived parameters may be overestimated. Though relatively noisy, the light curves favor a smaller radius in order to better match the steepness of the ingress and egress. The light curve fits imply a planetary radius of $1.25 \pm 0.15\ R_J$, which would correspond to a mass of $12.03 \pm 0.46\ M_J$. A precise trigonometric parallax measurement or a very accurate light curve is needed to resolve the uncertainty in the planetary mass and radius.

Subject headings: binaries: eclipsing — planetary systems — stars: individual (GSC 03727−01064) — techniques: photometric — techniques: radial velocities

Online material: color figures, machine-readable table

1. INTRODUCTION

There are now over 200 extrasolar planets known (Geneva Extrasolar Planet Search Programmes),[15] and most of these have been discovered using the radial velocity technique. As a result, most of these systems yield the minimum mass of the planet ($M_p \sin i$), its orbital semimajor axis, and properties of the central star. The data to date have dramatically changed our appreciation of the diversity of planetary systems that can form and have particularly focused the community's attention on the role that planetary migration plays in the planet formation process (see the review by Papaloizou et al. 2007). As the precision and duration of radial velocity surveys increase, lower mass planets and planets in longer orbits continue to be found. As a result, it has been suggested that the fraction of stars hosting planets may be as high as 50% (see Udry et al. 2007). Therefore, it appears that the planet formation process is relatively efficient.

The generally accepted model of giant planet formation is that of core nucleated accretion (e.g., Pollack et al. 1996; Bodenheimer et al. 2000; Hubickyj et al. 2005) in which gas giant planets first form a several (∼10) Earth-mass core of solids via nonelastic collisions in a disk followed by the runaway accretion of gas from the disk once the mass of the core is sufficient to exert a strong gravitational influence. Such a model naturally predicts a positive correlation between the metallicity of the disk (and parent star) and the ease with which planets can form: there are more building blocks to form the solid core in higher metallicity cases. The expected correlation has been suspected for some time (e.g., Gonzalez 1997; Santos et al. 2003) and has now been demonstrated in an unbiased way (e.g., Santos et al. 2004; Fischer & Valenti 2005) and has been taken as evidence in support of the core accretion model of planet formation. The competing model, gravitational instability in a massive circumstellar disk (e.g., Boss 1997, 2000; Mayer et al. 2002), does not predict such a relationship. Livio & Pringle (2003) showed that lower disk metallicity reduces the efficiency of Type II migration, which may account for some of the increased probability for finding a planet around more metal-rich stars. There is some observational evidence suggesting a higher frequency for planets at smaller separations

[1] Department of Physics and Astronomy, Rice University, 6100 Main Street, MS-108, Houston, TX 77005; cmj@rice.edu.
[2] Visiting Astronomer, McDonald Observatory, which is operated by the University of Texas at Austin.
[3] Space Telescope Science Institute, 3700 San Martin Drive, Baltimore MD 21218.
[4] Boston University, Astronomy Department, 725 Commonwealth Avenue, Boston, MA 02215.
[5] University of Hawaii, Institute for Astronomy, 2680 Woodlawn Drive, Honolulu, HI 96822.
[6] Lowell Observatory, 1400 West Mars Hill Road, Flagstaff, AZ 86001.
[7] Racoon Run Observatory, 1142 Mataro Court, Pleasanton, CA 94566.
[8] Volunteer Observatory, 10305 Mantooth Lane, Knoxville, TN 37932.
[9] Vermillion Cliffs Observatory, 4175 E. Red Cliffs Drive, Kanab, UT 84741.
[10] Esteve Duran Observatory, El Montanya, Seva, 08553 Seva, Barcelona, Spain.
[11] Hereford Arizona Observatory, 5320 E. Calle Manzana, Hereford, AZ 85615.
[12] Campo Catino Astronomical Observatory, P.O. Box 03016, Guarcino (FR), Italy.
[13] Bellatrix Observatory, Via Madonna de Loco, 47 03023 Ceccano (FR), Italy.
[14] CBA Belgium Observatory, Walhostraat 1A, B-3401 Landen, Belgium.
[15] http://exoplanets.eu/.

around metal-rich stars, which may support such a metallicity-migration relationship (Jones 2004; Sozzetti 2004). As a result, the planet-metallicity correlation may (at least in part) be due to a metallicity-migration relationship and may not simply signify a metallicity-formation relationship.

Additional observations of extrasolar planets are necessary to distinguish between the competing modes of planet formation and the conditions that affect planet migration scenarios. For example, the core accretion model requires several Myr to form Jovian planets in a disk (Inaba et al. 2003), while gravitational instabilities could potentially form these planets around very young stars. Jovian planets are suspected around a few $\sim$1 Myr young stars (e.g., CoKu Tau/4: Forrest et al. 2004; GQ Lup: Neuhäuser et al. 2005); however, clear detection and firm mass determinations from techniques such as radial velocity variations remain elusive on such young stars. Transiting extrasolar planets offer the opportunity to determine both the mass and radius of the planet and, hence, the planet's density. Such planets allow us to better constrain the variety of extrasolar planet properties and offer another potential way to distinguish between planet formation scenarios. For example, the high core mass derived for the transiting Saturnian-mass planet in orbit around HD 149026 (Sato et al. 2005) has been interpreted as strong support for the core accretion model. There are now $\sim$20 known transiting extrasolar planets (Geneva Extrasolar Planet Search Programmes). Several of these planets have unexpectedly large radii (see Fig. 3 of Bakos et al. 2007 and discussion therein), perhaps suggesting additional heating of these planets other than that from irradiation by the star they orbit. Additional effort is needed to understand the structure of extrasolar planets and their origins.

Here, we report the discovery of the third transiting planet from the XO Project. The XO Project aims to find planets transiting stars sufficiently bright to enable interesting follow-up studies (McCullough et al. 2005).[16] This planet presents some very interesting properties: it has a mass of $M_p \sin i = 13.02 \pm 0.64$ M_J and is in a short-period (3.2 day), eccentric orbit ($e = 0.260 \pm 0.017$) around the apparently single F5 V star GSC 03727−01064. XO-3b has a radius of 1.95 ± 0.16 R_J, making it substantially larger in both radius and mass than most of the other reported transiting planets. In § 2 we discuss the observations leading to the discovery of XO-3b. In § 3 we present our analysis of these observations to determine the stellar and planetary properties. In § 4 we give a discussion of XO-3b in the context of other extrasolar planets and current planet formation models, and we summarize our conclusions in § 5.

2. OBSERVATIONS

2.1. *XO Project Photometry*

McCullough et al. (2005) describe the instrumentation, operation, analysis, and preliminary results of the XO Project. In summary, the XO observatory monitored tens of thousands of bright ($V < 12$) stars twice every 10 minutes on clear nights for more than 2 months per season of visibility for each particular star, over the period 2003 September to 2005 September. From our analysis of more than 3000 observations per star, we identified XO-3 (Fig. 1) as one of dozens of stars with light curves suggestive of a transiting planet. With the XO cameras on Haleakala, we observed four transits or segments of transits of XO-3 in 2003 and three in 2004, on Julian dates 2,452,934, 2,452,937, 2,452,998, 2,453,001, 2,453,301, 2,453,320, and 2,453,352. Table 1 provides a sample of the photometry for XO-3 from the XO cameras. The full table is available in the online edition. From the survey photometry of XO-3 (Fig. 2), which has a nominal standard deviation of 0.8% or 8 mmag per observation, we determined a preliminary light curve and ephemeris, which we used to schedule observations of higher quality with other telescopes, as described in the next subsections.

[16] This paper includes data taken on the Haleakala summit maintained by the University of Hawaii, the Lowell Observatory, the Hobby-Eberly Telescope, the McDonald Observatory of the University of Texas at Austin, and five backyard observatories.

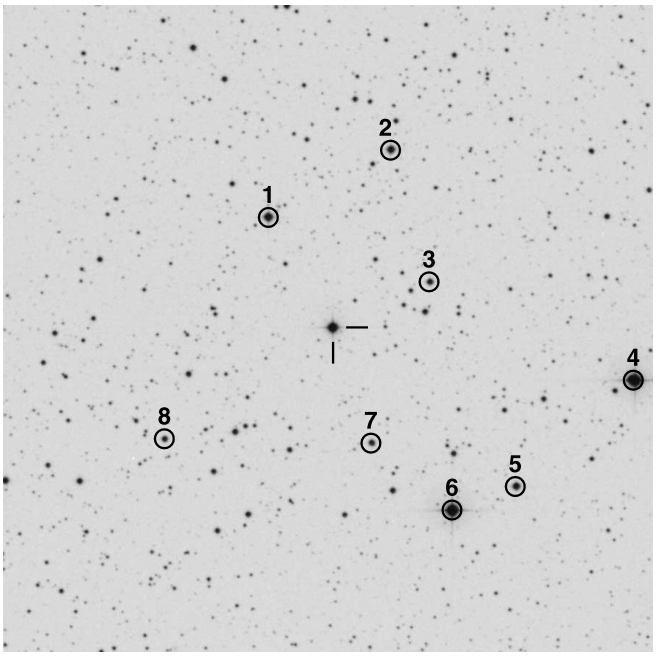

FIG. 1.—XO-3 is centered, indicated by the two hatch marks. Stars from Table 2 are circled. North is up; east to the left. The DSS image, digitized from a POSS II-F plate with a IIIaF emulsion and an RG610 filter, subtends 15′ of declination.

2.2. *Additional Photometry*

As outlined by McCullough & Burke (2007), once an interesting candidate is detedcted in the XO photometry, the candidate is released to an Extended Team (E.T.) of sophisticated amateur astronomers for additional observation. In 2006 September–November and 2007 January–March, transit events of XO-3 were observed by members of the E.T. from a total of four backyard observatories. Table 1 also provides E.T. photometry for XO-3. For the E.T. light curves, the median differential magnitude out of transit provides the flux normalization, and the standard deviation out of transit provides the uncertainty in the measurements. A fifth E.T. observatory was used to obtain all-sky photometry for XO-3. These observatories are equipped with telescopes of aperture $\sim$0.3 m. The telescopes, equipped with CCD detectors, are suitable for obtaining light curves sufficient to confirm the nature of the transit and obtain good timing information. A network of such telescopes is well suited to observe candidates with known positions and ephemerides. Here, we use two such telescopes in North America and two in Europe. Unlike the cases of XO-1b (McCullough et al. 2006) and XO-2b (Burke et al. 2007), we were not able to schedule observing time on a larger ($\sim$1 m) telescope to obtain additional photometry—the E.T. photometry is the best we have obtained to date on XO-3b (see Fig. 3).

We estimate all-sky photometric B, V, R_C, and I_C magnitudes for XO-3 and several nearby reference stars (Fig. 1 and Table 2) calibrated using a total of six Landolt areas (Landolt 1992). Using the Hereford Arizona Observatory (E.T. member B. L. G.) 0.36 m telescope on photometric nights 2006 October 27 and

TABLE 1
XO Survey and Extended Team Light-Curve Data

HJD	Light Curve (mag)	Uncertainty ($1-\sigma$) (mag)	Filter[a]	N[b]	Observatory
2,452,932.10913.....	−0.0017	0.0027	W	1	XO
2,452,932.10938.....	−0.0032	0.0026	W	1	XO
2,452,932.11597.....	0.0024	0.0026	W	1	XO
2,452,932.11621.....	0.0021	0.0025	W	1	XO
2,452,932.12305.....	−0.0016	0.0026	W	1	XO

Note.—Table 1 is published in its entirety in the electronic edition of the *Astrophysical Journal*. A portion is shown here for guidance regarding its form and content.

[a] The filters used in the XO project telescopes are described in McCullough et al. (2005). The bandpass is essentially flat from 4000 to 7000 Å.

[b] Average of N measurements.

2006 November 5, we measured the fluxes of 48 and 18 Landolt stars, respectively, at an air mass similar to that for XO-3 and established the zero points of the instrumental magnitudes and transformation equations for the color corrections for each filter and the CCD. The derived magnitudes for XO-3 differed on the two dates by 0.03 mag or less in all four colors. The B, V, R_C, and I_C absolute photometric accuracies are 0.03, 0.03, 0.03, and 0.05 mag rms, including both the formal error and an estimated systematic error. The Tycho magnitudes for XO-3 listed in Table 3 transform (via Table 2 of Bessel 2000) to Johnson $V = 9.86$, i.e., 0.06 mag (2 σ) fainter than our estimate.

2.3. *Spectroscopy*

In order to measure the orbital elements of the system, and in particular the mass ratio, as well as to determine the characteristics of the host star, we obtained spectra of XO-3 with two-dimensional cross-dispersed echelle spectrographs (Tull et al. 1995; Tull 1998) at the coudé focus of the 2.7 m Harlan J. Smith (HJS) Telescope and via a fiber optic cable on the 11 m Hobby-Eberly Telescope (HET). Both telescopes are located at McDonald Observatory. The HJS spectra were obtained in a traditionally scheduled manner, while the HET spectra were obtained in queue scheduled mode. An iodine gas cell is used on the HET to provide the wavelength reference for velocity determination. While an iodine cell is available for the HJS telescope, it is not a facility instrument, and the observations of XO-3 collected here were done as a part of a radial velocity survey of young stars (Huerta 2007; Huerta et al. 2008) for which very high (few m s^{-1}) velocity precision is not required. Wavelength and resulting velocity calibration is accomplished by taking thorium-argon reference lamp spectra before and after each observation of XO-3 at the HJS telescope. At the HJS we obtained one spectrum per night, and at the HET we obtained one or two spectra per night. At both telescopes, the spectral resolution was $R \equiv \lambda/\Delta\lambda \approx 60{,}000$, and data were obtained on a total of 21 nights. The two-dimensional echelle spectra were reduced using IDL procedures described in Hinkle et al. (2000), which include bias subtraction, flat-fielding using a quartz lamp spectrum, and optimal extraction of the data. Table 4 gives a log of the spectral observations.

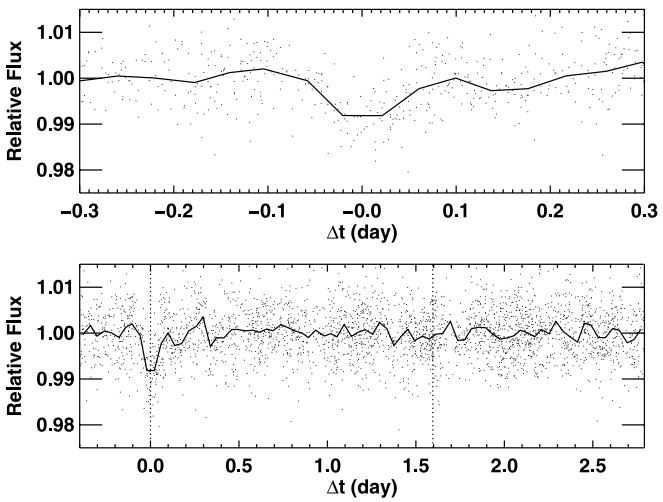

Fig. 2.—A total of 2969 individual observations of XO-3 by the two XO cameras over two seasons 2004 and 2005 are shown wrapped and phased according to the transit ephemeris and averaged in 0.01 day bins (*line*). The top panel is the full light curve, and the bottom panel shows the region around phase 0 (the primary transit, marked with a vertical dashed line in the top panel) enlarged. From these data we identified the star as a candidate for more refined photometry with other telescopes at epochs of expected transits (Fig. 3).

3. ANALYSIS

3.1. *Ephemeris*

We follow the same procedure used by Burke et al. (2007) for XO-2b to refine the ephemeris of XO-3b. We adopt the transit midpoint calculated for the event of 2006 October 16 as our ephemeris zeropoint: 2,454,025.3967 ± 0.0021. All measured transit midpoints used to refine the ephemeris are reported in Table 5. To determine the orbital period, we minimize the χ^2 difference between the observed transit times and a constant-period

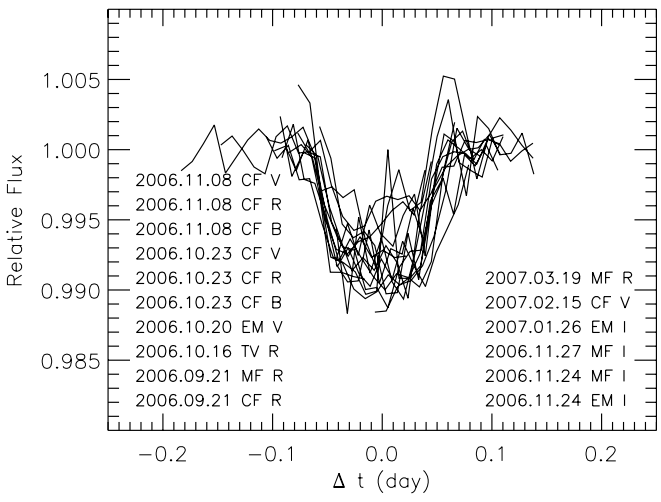

Fig. 3.—Time-series photometry of XO-3 from 2005–2007, with dates, observers, and filters indicated. The observations have been averaged in 0.006 day bins. [*See the electronic edition of the Journal for a color version of this figure.*]

TABLE 2
All-Sky Photometric Magnitudes

Star[a]	B	V	R_C	I_C
XO-3	10.25	9.80	9.54	9.28
1	11.37	10.82	10.50	10.18
2	12.38	11.62	11.17	10.76
3	14.81	13.07	12.17	11.30
4	10.13	9.03	8.43	7.88
5	12.67	11.87	11.43	10.92
6	9.26	8.78	8.50	8.21
7	15.52	13.46	12.41	11.50
8	15.34	13.84	12.59	11.51

[a] Stars are identified in Fig. 1.

ephemeris model. On the basis of three transit events observed either in multiple passbands by the same observer, or observed by different observers, we estimate the 1 σ uncertainty in the time of the center of an individual transit to be 5 minutes, which we adopt as the uncertainty for each of the transits observed in a single bandpass by only one observer. The best-fit period is 3.1915426 ± 0.00014 days.

3.2. *Radial Velocity Measurements*

Using spectra obtained at the HET, we measured XO-3's radial velocities with respect to the topocentric frame using iodine absorption lines superposed on the spectra of XO-3. We modeled the extracted spectra using a template stellar spectrum and the absorption spectrum of the HET iodine gas cell (Cochran 2000). For the analysis of XO-1 (McCullough et al. 2006) and XO-2 (Burke et al. 2007), a high-resolution spectrum of the Sun and the Earth's atmosphere (Wallace et al. 1998) was used for the template stellar spectrum. We followed this same procedure initially for XO-3; however, the resulting radial velocity uncertainties were substantially higher than we achieved for XO-1 and XO-2. We suspect that the higher $v \sin i$ of XO-3 compared to these other two stars contributes to this increased uncertainty, but we were also concerned that the higher temperature of XO-3 relative to these stars (and the Sun) resulted in spectral differences large enough to increase the uncertainty further. Therefore, we repeated the HET radial velocity determinations using a high-resolution ($\lambda/\delta\lambda \sim$ 60,000) spectrum of the F5 V star HD 30652 from the SPOCS sample of stars (Valenti & Fischer 2005, hereafter VF05) as the template stellar spectrum. The effective temperature of HD 30652 is 6424 K (VF05), within 5 K of our derived $T_{\rm eff}$ for XO-3 (see below), and $v \sin i = 16.8$ km s^{-1}, which is close to the value of 18.54 we find for XO-3 below. The spectrum of HD 30652 is very similar in appearance to that of XO-3.

Using an IDL[17] implementation of Nelder & Mead's (1965) downhill simplex χ^2 minimization algorithm, Amoeba, we adjusted parameters of our model spectrum to fit the observations. The model includes convolution of our model spectra with a best-fitting Voigt profile to approximate the (slightly non-Gaussian) line-spread function of the instrument. The free parameters of our model are a continuum normalization factor, the radial velocity of the star, the radial velocity of the iodine lines (which represent instrumental deviations from their expected zero velocity with respect to the observatory), and an exponent (optical depth scale factor) that scales the depths of the lines as an arbitrary method of adjusting the spectrum of HD 30652 to even more closely match that of XO-3. Due to the iodine absorption, we could not estimate the continuum level by interpolating between local maxima in the spectrum, so instead we solved for the continuum iteratively, as required to improve the fit between our model and the observations. In the manner described above, for each ~15 Å section of each individual spectrum within the region of the recorded spectrum with significant iodine absorption, 5100–5700 Å, we estimated the radial velocity of the star. From the approximately normal distribution of the resulting radial velocity estimates for each epoch, we calculated the mean radial velocity and its uncertainty. The 1 σ internal errors of the radial velocity measurements from the HET spectra range from ~120 to ~200 m s^{-1} per epoch. These uncertainties are an order of magnitude larger than those achieved on XO-1 (~15 m s^{-1}) and XO-2 (~20 m s^{-1}). We transformed our measured radial velocities to the barycentric frame of the solar system and subtracted the mean radial velocity and report these values in Table 4. These velocity measurements are shown in Figure 4.

The HJS radial velocity measurement technique used here is described in detail in Huerta (2007) and Huerta et al. (2008). We summarize it here. The radial velocity shift of each observed spectrum is determined by a cross-correlation analysis of the observed spectrum with respect to a reference spectrum. To avoid complications that might result from a spectral type mismatch,

[17] IDL is a software product of ITT Visual Information Solutions.

TABLE 3
The Star XO-3

Parameter	Value	Reference
R.A. (J2000.0)	$04^h21^m52.71^s$	1, 2
Decl. (J2000.0)	$+57°49'01.9''$	1, 2
V, V_T, $V_{\rm calc}$	9.80 ± 0.03, 9.904 ± 0.027, 9.86 ± 0.027	3, 2, 4
$B-V$, B_T-V_T, $(B-V)_{\rm calc}$	0.45 ± 0.04, 0.451 ± 0.040, 0.383 ± 0.034	3, 2, 4
$V-R_C$	0.26 ± 0.04	3
R_C-I_C	0.26 ± 0.06	3
J	9.013 ± 0.029	5
$J-H$	0.168 ± 0.034	5
$H-K_s$	0.054 ± 0.026	6
Spectral type	F5 V	3
d	260 ± 23 pc	3
(μ_α, μ_δ)	$(-0.6 \pm 2.7, 1.6 \pm 2.6)$ mas yr^{-1}	2
GSC	03727−01064	1

References.—(1) SIMBAD. (2) Tycho-2 Catalogue (Høg et al 2000). (3) This work. (4) Calculated from Tycho-2 measurements using standard transformations. (5) 2MASS (Skrutskie et al. 2006).

TABLE 4
Radial Velocity Shifts

HJD	Radial Velocity Shift (m s^{-1})	Uncertainty (1 σ) (m s^{-1})	$O-C$ (m s^{-1})	Bisector Span (m s^{-1})	Telescope
2,454,037.0112.....	1265	209	107	−31	HJS
2,454,038.0098.....	2001	216	174	4	HJS
2,454,137.8215.....	0	134	−92	0	HJS
2,454,138.8124.....	216	134	−112	170	HJS
2,454,139.8128.....	2625	139	−117	133	HJS
2,454,140.8131.....	267	139	−47	203	HJS
2,454,141.8047.....	77	149	13	112	HJS
2,454,142.7967.....	2761	139	−1	68	HJS
2,454,143.7999.....	881	143	242	42	HJS
2,454,144.7967.....	−35	161	34	152	HJS
2,454,005.8587.....	1454	129	103	...	HET
2,454,006.8597.....	−976	122	16	...	HET
2,454,113.5842.....	−71	184	44	...	HET
2,454,121.7100.....	−981	188	−43	...	HET
2,454,121.7190.....	−965	204	−16	...	HET
2,454,122.5635.....	−1152	182	52	...	HET
2,454,127.7046.....	−240	195	32	...	HET
2,454,128.7048.....	−1271	183	21	...	HET
2,454,158.6220.....	1191	144	−32	...	HET
2,454,159.6091.....	−278	132	−31	...	HET
2,454,162.6193.....	−30	194	−248	...	HET

we use one particular HJS epoch (2,454,137.8215) of XO-3 as the reference spectrum. Again, wavelength calibration is done by averaging the wavelength solution from thorium-argon reference lamps taken before and after each stellar observation. A total of 15 spectral orders that contain numerous, strong stellar lines, and no detectable telluric absorption lines are used in the cross-correlation analysis. The radial velocity shift from the 15 orders are averaged to get the final radial velocity shift for each observation, and the standard deviation of this mean is computed and adopted as the uncertainty of the cross-correlation analysis. Barycentric radial velocity corrections are then applied to the observations to determine accurate relative velocities for all the HJS spectra of XO-3.

TABLE 5
Transit Timing Measurements

UT Date	Observer	Filter	Transit Midpoint (HJD − 2,450,000.0)
2003 Dec 24	XO	W[a]	2997.72729
2004 Oct 22	XO	W[a]	3300.90479
2004 Nov 10.....	XO	W[a]	3320.05713
2004 Dec 12	XO	W[a]	3351.99341
2006 Sep 21.....	CF	*R*	3999.86011
2006 Sep 21.....	MF	*R*	3999.85913
2006 Oct 16.....	TV	*R*	4025.39673
2006 Oct 20.....	EM	*V*	4028.58984
2006 Oct 23.....	CF	*B*	4031.77759
2006 Oct 23.....	CF	*R*	4031.77954
2006 Oct 23.....	CF	*V*	4031.78052
2006 Nov 08.....	CF	*B*	4047.73022
2006 Nov 08.....	CF	*R*	4047.73804
2006 Nov 08.....	CF	*V*	4047.73340
2006 Nov 24.....	EM	*I*	4063.69019
2006 Nov 24.....	MF	*I*	4063.69897
2006 Nov 27.....	MF	*I*	4066.88525
2007 Jan 26.....	EM	*I*	4127.53076
2007 Feb 15.....	CF	*V*	4146.67725
2007 Mar 19	MF	*R*	4178.58936

[a] The filters used in the XO project telescopes are described in McCullough et al. (2005). The bandpass is essentially flat from 4000 to 7000 Å.

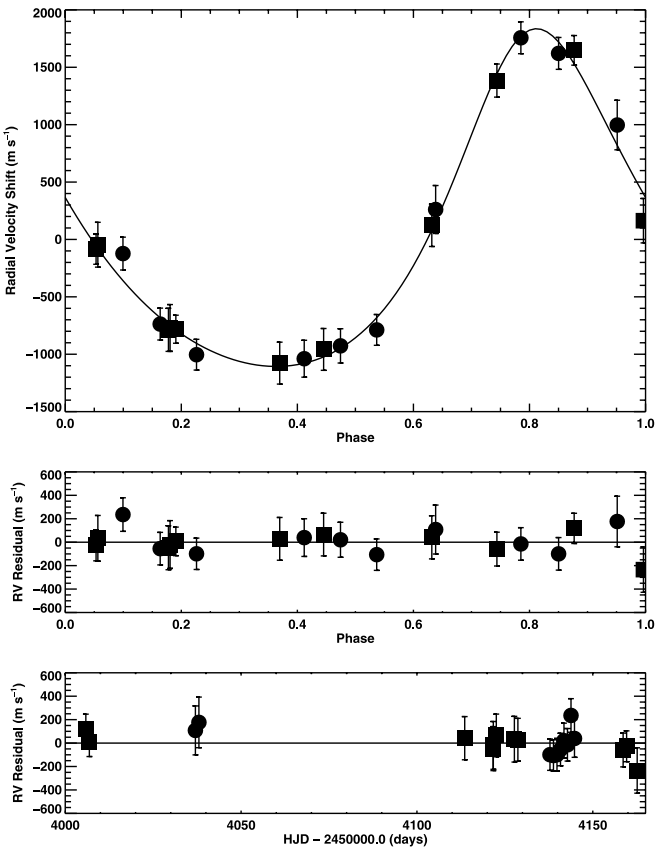

Fig. 4.—*Top:* The measured radial velocity data are shown along with the best-fit orbit. The filled circles are based on data from the 2.7 m Harlan J. Smith Telescope, and the filled squares come from data taken with the 11 m HET. The radial velocity curve of XO-3 traces out an eccentric orbit with a velocity amplitude $K = 1471 \pm 48$ m s^{-1}, implying XO-3b's mass is $M_p \sin i = 13.02 \pm 0.64\ M_J$. The period and phase used to fold the measured radial velocities are fixed at values determined by the photometric transits. The measured center-of-mass velocity with respect to the solar system's barycenter has been subtracted (its value is arbitrary since it is largely based on the intrinsically relative radial velocity measurements from the HJS). *Middle:* A plot of the radial velocity residuals, again phase folded with the ephemeris determined from the photometric transits. *Bottom:* The radial velocity residuals are shown again, this time as a function of time, showing no long-term trend.

In addition to the uncertainty found above from the order-to-order scatter in the HJS radial velocity measurements, there is an uncertainty associated with the fact that our wavelength calibration is based on spectra (thorium-argon) that are not observed simultaneously with the stellar spectrum as is the case for iodine cell observations. In order to evaluate this uncertainty, a total of six stars from the Lick Planet Search sample (Nidever et al. 2002; Butler et al. 1996; Cumming et al. 1999) that are known to be stable at the 5–20 m s^{-1} level are observed each night and analyzed in exactly the same way as we treat the spectra of XO-3. The internal uncertainty in the radial velocity shift measurements for these standard stars based on the measured order-to-order scatter is typically $<$20 m s^{-1}. For the 2007 February observing run (observations 3–10 at the HJS), the time series of radial velocity measurements for these standard stars show an average standard deviation of 123 m s^{-1}, with all but one of these stars showing a measured standard deviation $<$126 m s^{-1}. Therefore, we adopt the average value of 123 m s^{-1} as the uncertainty due to the nonsimultaneous nature of the HJS wavelength calibration for the 2007 February HJS observations of XO-3 and add it in quadrature to the uncertainty from the order-to-order scatter for each observation. For the 2006 October observations, the radial velocity standard-star data give an uncertainty of 132 m s^{-1} due to the nonsimultaneous nature of the target and wavelength calibration spectra. In addition, Huerta (2007) and Huerta et al. (2008) show that there are systematic offsets of the order of 100 m s^{-1} in the radial velocity standard-star measurements from one observing run to the next and speculate that this is caused by replacing the spectrometer slit plug between observing runs (the slit plug is not moved during the observing runs). Using the radial velocity standard-star data, we estimate that there is a systematic shift of 140 ± 33 m s^{-1} between the 2006 October and 2007 February observations. We correct our 2006 October radial velocity measurements of XO-3 by this amount and add this associated uncertainty in quadrature with the other radial velocity uncertainties described above. The measured radial velocity shifts and the total uncertainty are reported in Table 4 and shown in Figure 4 phased to the ephemeris known from the transits. The uncertainty for the radial velocity (=0 m s^{-1}) of the reference epoch (2,454,137.8215) is set equal to the lowest uncertainty determined for the other HJS relative radial velocity measurements.

An eccentricity approximately equal to zero is expected theoretically for hot Jupiters in $\sim$3 day orbits (Bodenheimer et al. 2001) and was our expectation for XO-3b. Therefore, we expected sinusoidal radial velocity variations for XO-3 with a phasing consistent with the transit observations. The first two observations obtained with the HJS, taken at phase $\sim$0.64 and $\sim$0.95, are inconsistent with this expectation, forcing us to consider eccentric orbits. Many additional data points are required to adequately constrain an eccentric orbit, so we performed intense observing of XO-3 with both the HJS and the HET in late 2006 and early 2007. When fitting the orbit, in addition to the radial velocity data, we also use the time of midtransit as a constraint in the fitting. Additionally, since the HJS and HET data are on different relative velocity scales, we treat as a free parameter the offset between these two scales. In the orbit fitting, we keep as fixed the orbital period and phases determined from the transit ephemeris and treat as free parameters the center-of-mass velocity of the system, the eccentricity, the velocity amplitude K for XO-3, the longitude of periastron, the phase of periastron passage, and the offset between the HJS and HET radial velocity measurements. We use the nonlinear least-squares technique of Marquardt (see Bevington & Robinson 1992) to find the best-fit parameters for the orbit, which are given in Table 6. Figure 4 shows the radial velocity data along with the orbital solution. In this plot, the HET data are shifted (by adding 1192.52 m s^{-1} to the HET radial velocities) to match the HJS spectra and the center-of-mass velocity (1002.68 m s^{-1}) of all points is subtracted for display purposes, since our center-of-mass velocity is based largely on only relative data. (As a result of these velocity shifts, the HJS velocities in Table 4 have had 1002.68 m s^{-1} subtracted from them for display in Fig. 4, and the HET velocities in Table 4 have had 189.84 m s^{-1} added to them for display in Fig. 4.) Uncertainties in the orbital fit parameters are derived by Monte Carlo simulation of the data: for 1000 simulations we construct fake radial velocity data using the orbital fit and applying Gaussian random noise at a level commensurate with the observed data and then fit this model data using the same procedure outlined above. Because the orbital fit produces a minimum reduced $\chi^2 = 0.53$, we believe our radial velocity uncertainty estimates may be a little too large. This can be seen in Table 4 where we report the observed minus calculated ($O-C$) velocities of the fit. These values are typically less than our derived uncertainties for the radial velocity measurements. The standard deviation of the HJS $O-C$ values is 122 m s^{-1} compared to a mean derived uncertainty of 156 m s^{-1}. For the HET data, the standard deviation of the $O-C$ values is 90 m s^{-1} compared to mean derived uncertainty of 169 m s^{-1} (though this is dominated by a single observation), indicating that the derived uncertainties for both data sets are too large. Reducing these uncertainties would reduce the uncertainties in the fit parameters, but we leave them as given, since we cannot justify any specific reduction in our measured radial velocity uncertainties. From the fit, we find that the velocity semiamplitude of the orbit of XO-3 is $K = 1471 \pm 48$ m s^{-1}.

As described below, the $v \sin i$ of XO-3 is relatively large, 18.5 ± 0.2 km s^{-1}, which is substantially larger than most stars around which planets have been discovered (HAT-P-2b is another example of a planet orbiting a star that has a relatively large $v \sin i = 19.8 \pm 1.6$ km s^{-1}; Bakos et al. 2007). The experience of Mandushev et al. (2005) and the similarity between the primary in that system and XO-3 give concern that XO-3 could be a hierachical triple system in which two lower mass stars comprise a short-period eclipsing binary star that are themselves orbiting a more massive, significantly brighter primary in a much longer period orbit. In the case of Mandushev et al. (2005), the short-period binary stars display tens of km s^{-1} velocity shifts, but the strong, broad lines of the system almost hide this signal. The apparent velocity shift of the system primary is then the result of weaker lines moving around the (stationary) lines of the primary,

TABLE 6
Orbital Solution and Planetary Parameters XO-3b

Parameter	Value	Notes
P	3.1915426 $\pm$ 0.00014 days	
t_c	2,454,025.3967 $\pm$ 0.0038 HJD	
e	0.260 $\pm$ 0.017	
ω	$-15.4^\circ \pm 6.6^\circ$	
T_0	2,454,024.7278 $\pm$ 0.0570 HJD	
K	1471 $\pm$ 48 m s^{-1}	
$M_p \sin i$	13.02 $\pm$ 0.64	1
R_p/R_s	(0.92 $\pm$ 0.04) $\times R_J/R_\odot$	2
i	$79.32^\circ \pm 1.36^\circ$	1, 3
a	0.0476 $\pm$ 0.0005 AU	1
M_p	13.25 $\pm$ 0.64 M_J	1, 4
R_p	1.95 $\pm$ 0.16 R_J	1, 2, 3

Note.—(1) For $M_* = 1.41 \pm 0.08\ M_\odot$. (2) $R_J = 71492$ km, i.e., the equatorial radius of Jupiter. (3) For $R_* = 2.13 \pm 0.21\ R_\odot$. (4) $M_J = 1.8988$E27 kg.

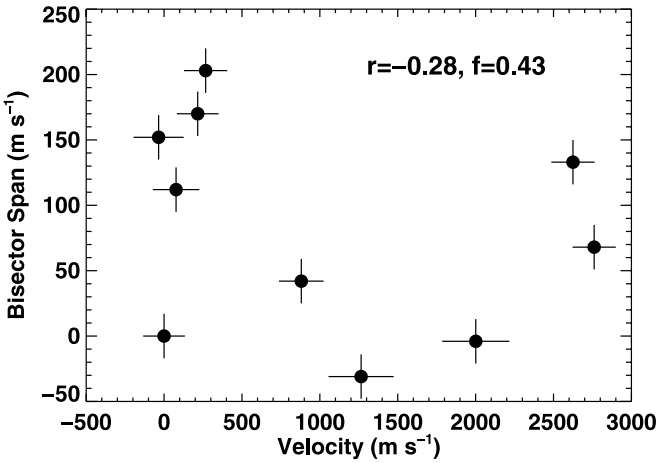

FIG. 5.—Bisector span, plotted as a function of the measured radial velocity for all the HJS spectra of XO-3. There is no correlation of the span with radial velocity, and the full amplitude of the span variations is less than a tenth of the full amplitude of the radial velocity variations.

producing line profile distortions that are misinterpreted as radial velocity variability of the primary.

Line bisector analysis is a standard technique to look for evidence that line distortions are producing false radial velocity variations (e.g., Hatzes et al. 1997; Martinez Fiorenzano et al. 2005) and have been used successfully to identify false radial velocity variations caused by star spots (e.g., Queloz et al. 2001; Bouvier et al. 2007; Huerta et al. 2008) and hierarchical triple systems (e.g., Santos et al. 2002; Mandushev et al. 2005). To improve the signal-to-noise ratio in bisector analysis, it is common practice to compute the bisector of the spectrum cross-correlation function (Queloz et al. 2001; Santos et al. 2002; Mandushev et al. 2005). Here, we calculate the line bisector of the total cross-correlation function computed from all 15 orders in the HJS spectra used in the determination of the radial velocities. We then compute the bisector span, which is the difference of the line bisector at two reference levels. Here we define the bisector span, S_B, as the value of the bisector at an absolute cross-correlation level of 0.15 minus the bisector at an absolute cross-correlation level of 0.75. These span values are given in Table 4. Because the spectral regions of the HET data that contain strong stellar lines also contain numerous iodine absorption lines, we restrict ourselves to the HJS data for the analysis of line bisectors. Previous studies that used bisector analysis to reveal a false positive in planet searches find a clear correlation between the measured radial velocity and the bisector span (Queloz et al. 2001; Santos et al. 2002; Mandushev et al. 2005; Bouvier et al. 2007; Huerta et al. 2008). In these cases, whether due to spots (e.g., Queloz et al. 2001; Bouvier et al. 2007; Huerta et al. 2008) or due to a hierarchical triple system (Santos et al. 2002; Mandushev et al. 2005), the full range measured in S_B is approximately the same as the full range of the measured radial velocities.

On the other hand, Torres et al. (2004) use the lack of a correlation between S_B and the radial velocity to help confirm a planet transiting OGLE-TR-56b. In addition, for OGLE-TR-56b the full range in S_B is less than one-third the full range in the radial velocities, which Torres et al. (2004) argue is additional evidence for the planetary nature of this object. Figure 5 shows the bisector span, S_B, plotted versus the measured radial velocity for the HJS spectra of XO-3. Also given in the figure is the value of the linear correlation coefficient and its associated false-alarm probability (Bevington & Robinson 1992) for these data. In addition to there being no significant correlation between S_B and the radial velocity, the full range of S_B is very small compared to the full range in the radial velocity. Figure 5 and Table 4 show that the full range in S_B in XO-3 is less than one-tenth the full range in the radial velocity variations for XO-3.

TABLE 7
RESULTS OF THE SME ANALYSIS

Parameter	Mean	Precision (1 σ)
$T_{\rm eff}$ (K)	6429	50
$\log g$ (cm s^{-2})	3.95	0.062
$V \sin i$ (km s^{-1})	18.54	0.17
[M/H]	−0.204	0.023
[Na/H]	−0.346	0.046
[Si/H]	−0.171	0.017
[Ti/H]	−0.262	0.049
[Fe/H]	−0.177	0.027
[Ni/H]	−0.220	0.033
[Si/Fe]	0.006	0.032

As a last check that the photometric dimmings and radial velocity variations of XO-3 are due to a planetary-mass companion and not the result of a hierarchical triple system with later type stars present, we looked for an infrared (IR) excess in XO-3. O'Donovan et al. (2006a) used a redder than expected $V - K$ measurement as one piece of evidence to reject the planetary hypothesis for the F star GSC 03885−00829. Using the photometry reported in Table 3, we estimate the color $V - K_s = 1.01 \pm 0.06$ for XO-3. On the basis of the effective temperature and gravity found below for XO-3, we assign a spectral type of F5 V based on the calibrations presented in Cox (2000). In the color system of Bessell & Brett (1988), an F5 V star such as XO-3 is expected to have an intrinsic $(V - K)_0 = 1.10$. For comparison to the 2MASS colors reported in Table 3, we use the color transformation relations found in the *Explanatory Supplement to the 2MASS All Sky Data Release and Extended Mission Products* by R. Cutri et al.[18] and find that we must add 0.039 mag to the Bessel & Brett value in order to estimate $(V - K_s)_0 = 1.14$ on the 2MASS system. Thus, the observed $V - K_s = 1.01$ color of XO-3 is 0.13 mag bluer ($\sim 2\,\sigma$) than its expected color. The slight bluing may be the result of the relatively low metallicity we derive (see below), but there certainly is no evidence for a near-IR excess suggesting a hierarchical triple system. The bisector analysis and the $V - K_s$ color of XO-3 give us confidence that both the photometric dimming and radial velocity variations we measure in this star are indeed due to a planetary-mass companion.

3.3. *Spectroscopically Derived Stellar Properties and Planetary Mass*

We used the software package SME (Valenti & Piskunov 1996) to fit each of the 10 spectra of XO-3 from the HJS telescope with synthetic spectra. We used the methodology of VF05, including their minor corrections to match the Sun and remove abundance trends with temperature (negligible in this case). Because of gaps between echelle orders, the HJS spectra are missing the wavelength interval 6000–6123 Å, which was included in the Valenti & Fischer analysis. This wavelength interval is also missing from our extracted HET spectra because the relevant echelle orders span the gap between the two detectors.

We averaged our SME results for the 10 HJS spectra, obtaining the parameter values in Table 7. Each value in the last column

[18] http://www.ipac.caltech.edu/2mass/releases/allsky/doc/.

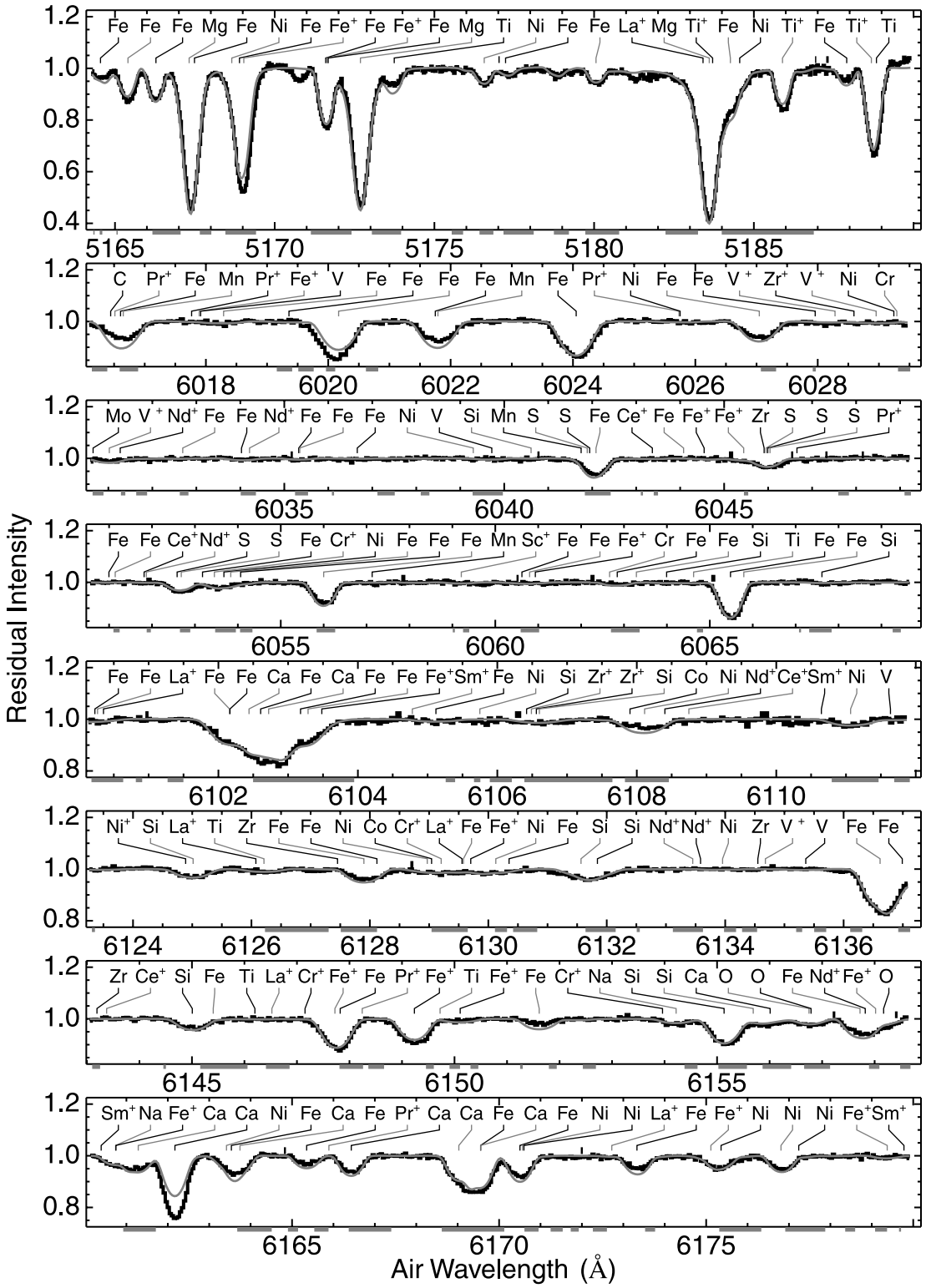

FIG. 6.—Mean spectrum of XO-3 as observed (*black histogram*) and modeled with SME (*blue curve*) in the region of the Mg *b* triplet. Labels note the elements responsible for the indicated spectral lines. Intermittent line segments (*tan*) beneath the horizontal axis indicate wavelength intervals used to constrain the spectroscopic parameters. Very short and intermittent line segments (*black*) immediately above the spectrum indicate wavelength intervals used to constrain the continuum fit. [*See the electronic edition of the Journal for a color version of this figure.*]

of the table, labeled "Precision" because systematic uncertainties are not included, is the standard deviation of the 10 measurements divided by $\sqrt{9}$ to yield the formal uncertainty in the mean. The median value of each derived parameter (not given) differs from the mean by less than the uncertainty in the mean. The final row in the table gives [Si/Fe], which VF05 used as a proxy for α-element enrichment, when interpolating isochrones. Figure 6 shows XO-3's spectrum in the region of the Mg I B triplet, which is the dominant spectroscopic constraint on gravity. These three Mg lines also have a significant impact on the global [M/H] parameter, which is used to scale solar abundances for all elements other than Na, Si, Ti, Fe, and Ni.

TABLE 8
SPECTROSCOPICALLY DERIVED STELLAR PARAMETERS

Parameter	240 pc	260 pc	280 pc
Mass ($M_\odot$).....	1.33	1.36	1.39
	1.36	1.41	1.43
	1.39	1.44	1.48
Radius ($R_\odot$).....	1.92	2.08	2.22
	1.95	2.13	2.27
	1.99	2.17	2.34
$\log g$ (cm s^{-2}).....	3.98	3.93	3.87
	4.00	3.95	3.89
	4.02	3.97	3.91
Age (Gyr).....	2.66	2.53	2.41
	2.78	2.69	2.68
	3.06	2.83	2.96

NOTE.—For each parameter, the middle row is the maximum likelihood value, and the values in the rows above and below span the 68% likelihood of the probability distributions (cf. Fig. 7). The three columns correspond to three assumed distances for XO-3.

Following the methodology of Fischer & Valenti (2005), we interpolated Yonsei-Yale (Y^2) isochrones (Demarque et al. 2004) to determine probability distribution functions for the mass, radius, gravity, and age of XO-3. The trigonometric parallax of XO-3 is unknown, so we initially assumed distances of 240, 260, and 280 pc with an adopted uncertainty of 10 pc in each case (which affects the width of the resulting distribution functions) (see Table 8). In order to perform the isochrone analysis, we need a V magnitude corrected for extinction for XO-3. We measured $V = 9.80 \pm 0.03$ and $B = 10.25 \pm 0.03$ for XO-3 (Table 3). These observations give a measured $B - V = 0.45 \pm 0.04$ for XO-3. VandenBerg & Clem (2003) determined empirical color-temperature relations for stars including variations with gravity. We downloaded their high-temperature table (mentioned in footnote 1 of their paper) and interpolated in the table to the effective temperature, surface gravity, and metallicity of XO-3 determined above. Doing so gives a predicted $(B - V)_0 = 0.440$ for XO-3. As discussed below, the light-curve analysis and the derived properties of XO-3b favor a larger stellar gravity for XO-3. So, we also interpolate the predicted colors to a gravity of $\log g = 4.2$ (a little more than 3 σ higher than the spectroscopically derived value). Doing so results in a predicted $(B - V)_0 = 0.446$. These two

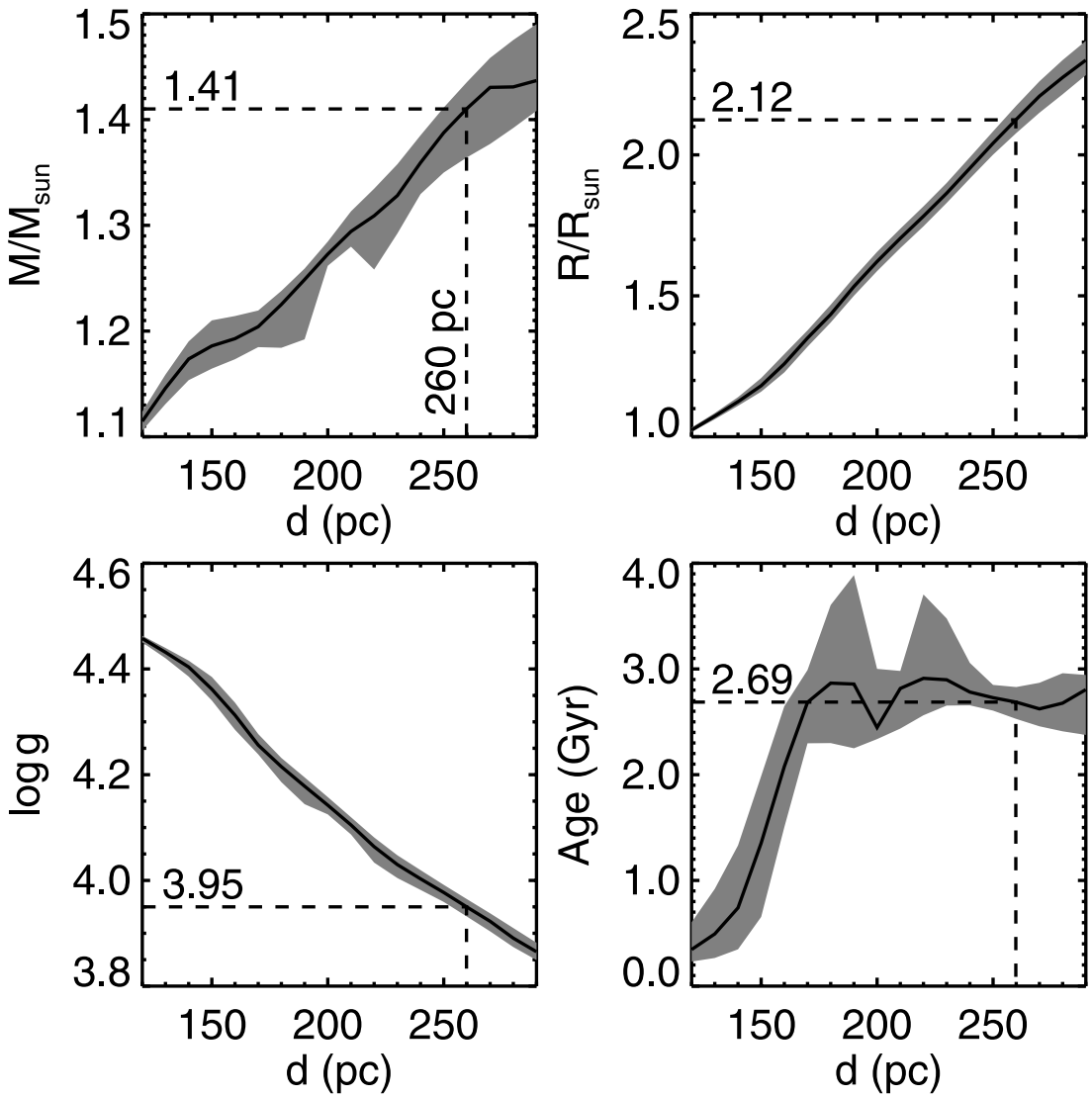

FIG. 7.—Stellar mass, radius, gravity, and age that result from the isochrone analysis. The solid line shows the derived values as a function of the assumed distance, and the gray region shows the 68% confidence limit on these parameters. Dashed lines are drawn at 260 pc corresponding to the spectroscopically determined $\log g = 3.95$.

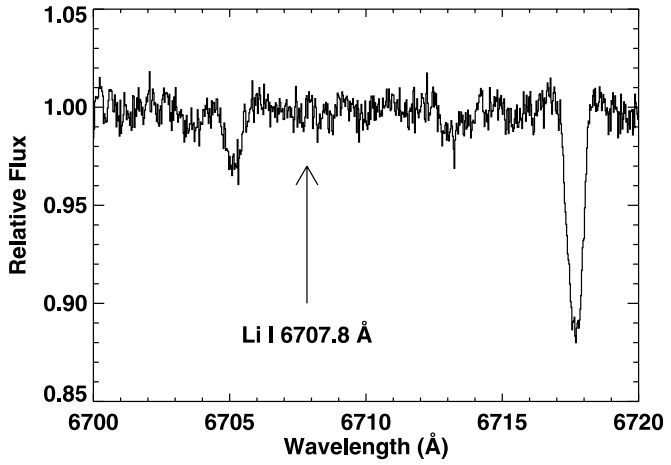

FIG. 8.—Spectrum of XO-3 in the wavelength region of the Li I doublet at 6708 Å. The position of the Li feature is marked. The Li feature is expected to be approximately as strong as the Ca I line at 6718 Å in Pleiades age stars of similar spectral type and even stronger at younger ages. Therefore, we conclude that XO-3 is not a pre–main-sequence star but instead is likely on the post–main sequence.

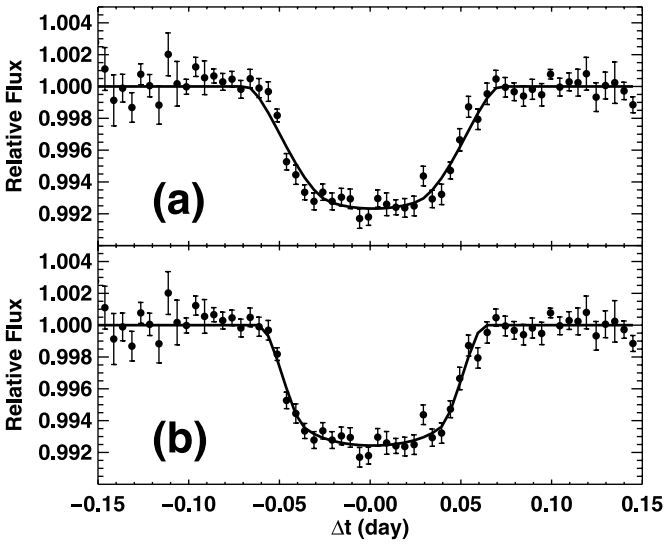

FIG. 9.—Combined E.T. transit light curve of XO-3 and the best-fit transit light-curve models computed under different assumptions. Panel *a* fixes the stellar mass and radius to the values determined from the combined spectroscopic and isochrone analysis. Panel *b* is determined by minimizing χ^2 in the light-curve fit by letting the stellar mass and radius vary according to the isochrone results for different assumed distances. This best fit produces a stellar gravity ($\log g$) more than 3 σ greater than the measured value from the spectroscopic analysis.

predicted values are within 0.01 and 0.001 mag of the measured $B - V$ of XO-3, with an uncertainty of 0.04 in the measured color. We therefore find no compelling evidence for significant reddening to XO-3, and we adopt $V = 9.80 \pm 0.03$ as the extinction-corrected magnitude of the star.

We used our spectroscopic effective temperature, spectroscopic gravity, and an assumed distance to derive a bolometric correction by interpolating the "high-temperature" table from VandenBerg & Clem (2003). We combined the bolometric correction with the observed *V*-band magnitude to determine stellar luminosity. Then we used the stellar luminosity and our spectroscopic effective temperature, iron abundance, and α-element enrichment to interpolate the Y^2 isochrones to produce the probability distribution functions in Figure 7.

The parameters we derive place XO-3 above the zero-age main sequence. As a result, reasonable fits to the data are possible for pre–main-sequence evolutionary tracks. However, if XO-3 were indeed a pre–main-sequence star, we would expect strong Li I absorption at 6708 Å. For example, in their survey of Pleiades F stars, Boesgaard et al. (1988) show that the Li I line at 6708 Å is approximately as strong as the nearby Ca I line at 6718 Å in stars of similar spectral type to XO-3. We show in Figure 8 the Li line region in XO-3 produced by averaging the spectra obtained at the HET (this region is free of iodine absorption). The position of the Li I line is marked and the nearby Ca I line is clearly visible. The Li line is not detectable, indicating that XO-3 is substantially older than the Pleiades; therefore, we conclude that XO-3 is not a pre–main-sequence star.

The most probable distance, mass, radius, and age for XO-3 are 260 pc, 1.41 $M_\odot$, 2.13 $R_\odot$, and 2.69 Gyr, respectively, for our best-fit gravity of $\log g = 3.95$. Combined with our measured semiamplitude $K = 1471 \pm 48$ m s^{-1}, this stellar mass implies a mass of $M_p \sin i = 13.02 \pm 0.64$ M_J for the planet XO-3b. If we assume that XO-3 is at 240 pc instead, then the most probable mass, radius, age, and gravity are 1.36 $M_\odot$, 1.95 $R_\odot$, 2.78 Gyr, and $\log g = 4.00$, still placing the star well above the main sequence. As discussed below, one of the unusual properties of XO-3b is the relatively large radius we derive for the planet. The planetary radius is approximately proportional to the inferred stellar radius. The planetary radius could be smaller if we could justify a smaller stellar radius; however, doing so begins to bring the inferred gravity in conflict with the spectroscopically derived value of $\log g = 3.95 \pm 0.062$. Taking a 3 σ upper limit, the largest allowed value for the gravity is $\log g = 4.14$, corresponding to a stellar mass of 1.27 $M_\odot$ and a stellar radius of 1.62 $R_\odot$ for an inferred distance of 200 pc. Together with the measured velocity semiamplitude, these values imply a planetary mass of $M_p \sin i = 12.14 \pm 0.40$ M_J, where the uncertainty here is just that resulting from the radial velocity fit. Clearly, a trigonometric parallax measurement for XO-3 will be of great value in better establishing both the stellar and planetary parameters.

3.4. *Light-Curve Modeling and the Planetary Radius*

For additional photometric analysis and light-curve fitting, all the E.T. photometric data shown in Figure 3 were averaged into 7.4 minute bins. Binning permitted outlier rejection and empirical estimation of the noise by the scatter of the individual observations, which is helpful in cases such as this in which residual calibration errors can be significant. Differences in the depth and the shape of the transit light curve in different photometric bands are both expected and observed to be substantially smaller than the photometric uncertainties in the E.T. light curves, so we combined the light curve from all photometric bands to improve the signal-to-noise ratio. The binning begins with phasing the light curves using the refined ephemeris determined in § 3.1. The final binned light curve consists of a robust average of E.T. photometric measurements in bins 7.4 minutes in duration. This robust average is determined by first calculating the median and median absolute deviation for each bin and rejecting points in the bin that deviate by more than 4 σ from the median. Next, the mean and standard deviation are calculated for each bin, and points that are more than 4 σ from the mean are rejected. This rejection based on the mean and standard deviation is repeated one more time before a final ("robust") mean is calculated. The final binned light curve is supplied in Table 1 and is shown in Figure 9 along with the fits described below. The uncertainty in each binned light-curve data point is the standard deviation of (surviving) measurements in the bin divided by the square root of the number of measurements in that bin. The uncertainties in all bins are then

multiplied by a correction factor as described below (the uncertainties in Table 1 do not have this correction factor applied).

We modeled the mean transit light curve using the analytic transit model of Mandel & Agol (2002). For a planet with an eccentric orbit, the transit model has 10 parameters: transit midpoint (t_0), orbital period, stellar mass (M_*), stellar radius (R_*), planet radius (R_p), inclination (i), quadratic limb-darkening law coefficients (u_1 and u_2), eccentricity (e), and longitude of perihelion (ω). Throughout the following analysis, the orbital period remains fixed at the period found in § 3.1. The radial velocity data provide the best estimates for $e = 0.26$ and $\omega = -2.64$ that remain fixed during the χ^2 minimization. For each fit presented below, we fix the stellar parameters to specific values based on the spectral synthesis and isochrone analysis presented above. We interpolate quadratic limb-darkening coefficients from Claret (2000) for the Cousins R photometric bandpass ($u_1 = 0.220$; $u_2 = 0.380$) based on the gravity, effective temperature, and metallicity ([M/H]) determined from the spectroscopic analysis (Table 7). The remaining parameters, t_0, R_p, and i, are allowed to vary and are solved for using the Amoeba algorithm mentioned earlier. For input into the Mandel & Agol (2002) transit model, we determine the projected separation between star and planet, δ, in the case of nonzero eccentricity following the procedure outlined by Hilditch (2001). For a given i, ω, and e, we determine the true anomaly, $\theta_{\min}$, that minimizes δ (eq. [4.9] of Hilditch 2001). The resulting $\theta_{\min}$ corresponds to the mean anomaly at transit midpoint providing the zero point to convert observed times to θ via Kepler's equation.

We then initially fit the light curve assuming the stellar mass ($1.41\ M_\odot$) and radius ($2.13\ R_\odot$) derived from the spectral fits as described above. The free parameters of the light-curve fit are then the radius of the planet and the inclination of the orbit (and the time of midtransit). The resulting fit is shown in the top panel of Figure 9. We then repeated the light-curve fits using the extremes in the stellar mass (1.33 and $1.90\ M_\odot$) and radius (1.49 and $2.36\ R_\odot$) that result from the 1 σ uncertainties in these parameters derived above. Together, this then gives us estimates of the planetary radius ($R_p = 1.95 \pm 0.16\ R_J$) and orbital inclination ($i = 79.32^\circ \pm 1.36^\circ$), which are also given in Table 6. The total mass of the planet is then $13.25 \pm 0.64\ M_J$. Examination of the figure shows that the model does not fit all aspects of the light curve: the model ingress and egress appear noticeably longer than the observed ingress and egress.

In order to better model the shape of the ingress and egress while still maintaining the total duration of the transit, the radius of the star and the planet both need to be reduced and the inclination must increase so that the total chord length the planet traverses across the face of the star stays approximately the same. Figure 7 shows that from the isochrone analysis, the stellar mass and radius both decrease as the distance is assumed to be smaller. We have performed the isochrone analysis every 10 pc, so we computed model light curves, stepping down in distance 10 pc at a time from our favored distance of 260 pc. For each new distance, we adopt the corresponding stellar mass and radius resulting from the isochrone analysis and compute χ^2 for the fit to the light curve. The minimum in χ^2 occurs between 190 and 200 pc. Fitting a parabola to the lowest four χ^2 values gives a best fit to the light curve for a distance of 185 pc, which gives $M_* = 1.24\ M_\odot$, $R_* = 1.48\ R_\odot$, and $\log g = 4.19$. This fit is shown in the lower panel of Figure 9. As mentioned earlier, the best χ^2 is quite large ($\sim$129) for the 63 degrees of freedom in our fit, indicating that the photometric uncertainties have been underestimated. We attempt to correct this by determining the multiplicative factor required to give a $\chi^2 = 63.0$ (a reduced $\chi^2 = 1.0$). The uncertainties shown in Figure 9 have been multiplied by this factor. Having done this, we can then assign as the uncertainty in R_P and i the difference between the best-fit parameters and those we obtain when $\Delta\chi^2 = 1.0$. Doing so, we find that the transit light curve is best fit for $R_p = 1.25 \pm 0.15\ R_J$ and $i = 83.32^\circ \pm 1.26^\circ$. The total mass of the planet is then $12.03 \pm 0.46\ M_J$. This value for the planetary radius is considerably lower than the value derived above from the default stellar parameters. As discussed below, we regard this as a lower limit to the true planetary radius; however, we note that the ambiguity described here can be greatly diminished by obtaining very accurate photometry of a transit of XO-3 and/or by obtaining a precise trigonometric parallax measurement.

4. DISCUSSION

4.1. *Comparison to Other Transiting Planets*

The $\sim$13 M_J planet XO-3b is unusual in many respects compared to the sample of known extrasolar planets. The mass of XO-3b is quite large compared to most of the known extrasolar planets. Zucker & Mazeh (2002) noted that the most massive short-period planets are all found in multiple-star systems. Udry et al. (2003) emphasized the general lack of massive planets on short-period orbits, particularly for planets orbiting single stars, and interpreted these results in terms of planetary migration scenarios. The star XO-3 is not known to be a binary, though it is relatively unstudied. While it is in the Tycho-2 catalog (Høg et al. 2000), XO-3 does not have a significant proper-motion measurement from the *Hipparcos* mission. It is not known if any of the nearby stars seen in Figure 1 are common proper-motion companions or not. Udry et al. (2003) point out that among planets orbiting single stars known at that time, there were no planets more massive than $2\ M_J$ with periods less than 100 days (see also Eggenberger et al. 2004). Using data for 218 extrasolar planets as compiled on the Geneva Extrasolar Planet Web site updated as of 2007 May 27, this general lack of short-period, very massive planets is still apparent. There are only three other planets (HD 162020b, HD 17156b, and HAT-P-2b) orbiting apparently single stars with periods less than 30 days and masses larger than $2.5\ M_J$, and one of those (HD 162020b) is suspected to actually be a much more massive brown dwarf (Udry et al. 2002). There is only one planet other than XO-3b with a mass larger than $2.5\ M_J$ and a period less than 4 days (HD 120136b, $M_2 \sin i = 4.14\ M_J$; Butler et al. 1997), and this star is known to be in a stellar binary system (Hale 1994).

The eccentricity of XO-3b is also quite rare relative to other known extrasolar planets, given the short orbital period of XO-3b. The eccentricity of the shortest period extrasolar planets are all quite low ($e < 0.05$), and most are consistent with zero eccentricity (Halbwachs et al. 2005). This is generally believed to be either due to tidal circularization (e.g., Wu 2003; Ivanov & Papaloizou 2007) or the result of smooth orbital migration in a disk that is not thought to produce significant eccentricity (Murray et al. 1998). The eccentricity of XO-3b is larger than all other planets with periods less than that of XO-3b. We discuss the eccentricity of XO-3b further in § 4.3. While the mass, period, and eccentricity of XO-3b make it quite rare among extrasolar planets, it is not totally unique. The recently discovered HAT-P-2b (Bakos et al. 2007) is very similar in many respects with a period of 5.6 days, $M_p = 9.04\ M_J$, and $e = 0.52$. Also, the hot Neptune GJ 436b has a period of 2.6 days and $e = 0.15$ (Butler et al 2004; Deming et al 2007). Apparently the assumption, commonly held prior to 2007, that short-period planets should have circular orbits was incorrect.

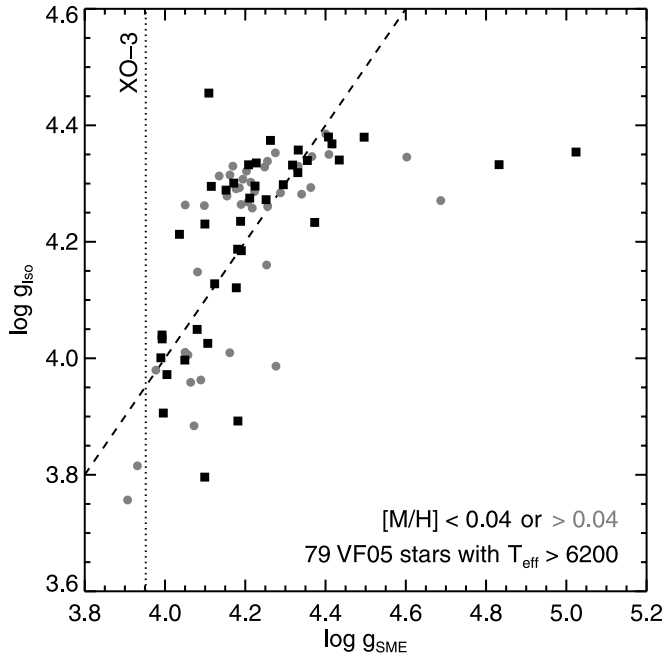

FIG. 10.—Comparison of spectroscopically derived gravities to those derived from isochrone analysis for the sample of stars from VF05 that have effective temperatures similar to XO-3. Stars with [M/H] < 0.04 are shown as blue squares, and those with [M/H] > 0.04 are shown with red circles. The green dashed line is the line of equality. [*See the electronic edition of the Journal for a color version of this figure.*]

It is now well established that host-star metallicity correlates with the likelihood of finding a Jupiter-mass companion orbiting the star in the sense that higher metallicity stars are more likely to have planets (Santos et al. 2004; Fischer & Valenti 2005). The metallicity of XO-3 ($[M/H] = -0.20$) is relatively low, and the above-mentioned studies show that planets are found around only ~3% of stars with similar metallicity. There are only two other very massive planets ($M_p > 5\ M_J$) known around stars (HD 111232, HD 114762) with metallicities lower than that of XO-3. The correlation between host-star metallicity and the probability of finding a planet is often taken as support for the core accretion model (e.g., Pollack et al. 1996; Bodenheimer et al. 2000; Hubickyj et al. 2005) of planet formation. Under that assumption though, it may be surprising that a few very massive planets have also been found around low-metallicity stars. It has also been suggested that host-star metallicity decreases on average as the planet mass increases, which appears inconsistent with the core accretion model (Ribas & Miralda-Escudé 2007). On the other hand, gravitational instabilities in a disk are not expected to produce a metallicity-planet correlation (Boss 2002). Taking this notion further, Ribas & Miralda-Escudé (2007) have suggested that the sample of extrasolar planets consists of objects formed via two different paths: core accretion in a disk and fragmentation of a prestellar cloud. The high mass, relatively large eccentricity, and low metallicity of the XO-3b system would then "fit" the notion of Ribas & Miralda-Escudé of a planet formed from the collapse of a prestellar cloud, but of course the observations of XO-3b do not prove (or disprove) either formation scenario.

4.2. *How Big Is XO-3b?*

Potentially, one of the most unusual and interesting properties of XO-3b is the large radius of the planet. At an age of 2–3 Gyr, giant planets and low-mass brown dwarfs are expected to have radii very close to that of Jupiter (Burrows et al. 2001; Baraffe et al. 2003). Using the tables in Baraffe et al. (2003), the radius of a 13 M_J planet is expected to be 1.03 R_J at 1 Gyr and 0.97 R_J at 5 Gyr. Including heating from the central star can increase the expected radius for so-called hot Jupiters (e.g., Bodenheimer et al. 2003). Fortney et al. (2007) compute planetary structure models up to 11.3 M_J for a range of orbital separations, including the insolation produced by absorption of solar radiation. At an age of 300 Myr or older, all the models computed have radii less than 1.3 R_J. In all cases analyzed by Fortney et al., their models predict a substantially smaller radius than the $1.95 \pm 0.16\ R_J$ determined based on the values of the stellar mass and radius inferred from the spectroscopic and isochrone analysis of XO-3. Such a large discrepancy between the observed and predicted planetary radius is reminiscent of TReS-4, which has a radius of $1.674 \pm 0.094\ R_J$ (Mandushev et al. 2007). However, the radius of XO-3b is quite uncertain, and the light curve itself favors a smaller planetary radius of $R_p = 1.25 \pm 0.15\ R_J$. Because XO-3b is in an eccentric orbit, for comparison with the models of Fortney et al. (2007) we compute the average orbital separation between XO-3b and its star and then adjust this separation to take into account the difference in luminosity between XO-3 and the Sun. The smaller planetary radius for XO-3b is associated with a smaller stellar radius for XO-3, so for this exercise, we take $R_* = 1.57\ R_\odot$. We thus compute an effective distance of 0.024 AU to use for XO-3b when using the tables of Fortney et al. (2007). Interpolating in these tables, the predicted radius for XO-3b is 1.18 R_J at 1 Gyr and 1.11 R_J at 4.5 Gyr. Both values are lower than the smaller radius inferred for XO-3b, but only by about 1 σ. A more precise radius for XO-3b would be a very interesting benchmark for the theory of extrasolar planets.

The actual radius of XO-3b can be better constrained by a true parallax measurement and more precise photometric observations (ideally in multiple colors) of additional transits. The constraint from this work that favors the larger radius for XO-3b is the stellar gravity inferred from the spectroscopic analysis. A number of investigators have pointed out that stellar gravity determinations are notoriously difficult, and the relative error in this parameter is often substantially larger than almost all other measured properties of transiting extrasolar planetary systems. Many of these investigators have elected to use the transit light-curve fits in combination with stellar isochrone models to estimate the stellar and planetary radius and hence $\log g$ for the star (e.g., Sozzetti et al. 2004, 2007; O'Donovan et al. 2006b; Bakos et al. 2007; Mandushev et al. 2007). The photometry of XO-3b is not as precise as that used in those studies, so we do not emphasize the photometrically derived parameters as those investigators have. However, we can examine the spectroscopically determined $\log g$ to estimate by how much, and in what sense, it is in error.

The above studies typically use spectroscopically determined effective temperatures with isochrone models to determine the stellar gravity, implicitly assuming the gravities determined from isochrone analyses are more accurate than the spectroscopic values. We can compare the gravities determined from the Y^2 isochrones and our spectroscopic analysis for stars of similar spectral type to XO-3. The sample of stars studied by VF05 all have accurate *Hipparcos* parallax measurements, allowing them to use the isochrones with the spectroscopically determined $T_{\rm eff}$ to determine the stellar gravity. This gravity can then be compared to the gravity VF05 derive from the spectra alone, using the same techniques used in this paper. Figure 10 shows the result of this comparison for 79 stars with $T_{\rm eff} > 6200$ K from VF05. Recall $T_{\rm eff} = 6429 \pm 50$ K for XO-3. There is considerable scatter in this figure; however, in the immediate vicinity of the spectroscopic gravity determined

for XO-3, the gravities determined from the isochrones are lower. This is the opposite sense to what is suggested by the transit light curve of XO-3. As a result, there is no clear indication in this sample of stars that the spectroscopically determined gravity for XO-3 is biased low. When making this comparison, it is appropriate to consider the accuracy of the gravities predicted by the Y^2 isochrones. Hillenbrand & White (2004) report excellent agreement (better that 3%) between dynamically determined stellar masses from eclipsing binaries and masses determined from the Y^2 isochrones for main-sequence stars more massive than $\sim 0.6\ M_\odot$; therefore, we find no reason to doubt the Y^2 isochrones appropriate for XO-3. We also note that results from transit light-curve analyses are subject to various assumptions and potential biases that may exist in the models used for the fit. For example, Aufdenberg et al. (2005) confirm the prediction of Allende Prieto et al. (2002) that 1D atmosphere models, including the ATLAS models used by Claret (2000) to determine limb-darkening coefficients, predict too much limb darkening at optical wavelengths, depending on the treatment of convection and convective overshoot in the model. In fitting light curves, such a bias will favor models with smaller impact parameters and smaller stellar radii. Therefore, until better data can be obtained for XO-3 (a precise parallax measurement and/or more precise transit photometry), the stellar and hence planetary radius will remain significantly uncertain. At this point, taking the photometric light curve and the spectroscopic gravity into account, we estimate the radius of XO-3b to be $1.10 < R_p < 2.11\ R_J$ including $1\ \sigma$ uncertainties on both limits. The lower limit is almost certainly too low however, given the results of Aufdenberg et al. (2005) and Allende Prieto et al. (2002) on limb darkening showing that the values we have used here are likely overestimated.

4.3. *Tidal Circularization and the Eccentricity of XO-3b*

As mentioned in § 4.1, an interesting aspect of the orbit of XO-3b is its significant eccentricity, $e = 0.260 \pm 0.017$, because most planets with orbital periods similar to XO-3b are believed to have already been tidally circularized (Halbwachs et al. 2005). Independent of exactly how XO-3b arrived at its current orbit, it is interesting to consider how long it can remain in such an orbit under the influence of tidal circularization. The question of tidal circularization of close extrasolar planets has been studied by several investigators (see Adams & Laughlin 2006 and references therein). The equations governing the tidal circularization of extrasolar planets depend on very uncertain planetary quality factors, Q_p (for example, see the discussion in Gu et al. 2003) and in some cases equally uncertain stellar quality factors, Q_*, if considering tides raised on the star by the planet. As an illustration of the difficulty in estimating quality factors, Mathieu (1994) points out that theoretically determined values of Q_* imply a slow rate for close binary stars to circularize that is contradicted by observations in stellar clusters of various ages. As a result, many investigators try to use the observations (of binary stars and extrasolar planets) to empirically estimate the quality factors. For Jupiter-mass extrasolar planets, $Q_p \sim 10^5$–10^6 (e.g., Gu et al. 2003; Adams & Laughlin 2006).

Circularization timescales depend linearly on Q_p, so we assume $Q_p = 10^6$ to get predictions at the long end of what can currently be estimated. Using equation (18) of Gu et al. (2003) and equation (3) of Adams & Laughlin (2006) to estimate the circularization time for XO-3b, we find timescales of 0.29 Gyr and 0.33 Gyr, respectively, using values corresponding to the large radius ($1.9\ R_J$) for XO-3b. The circularization timescale in both studies depends on the reciprocal of the planetary radius to the fifth power, so the circularization timescale grows to 2.92 Gyr and 3.32 Gyr, respectively, using values corresponding to the small radius ($1.32\ R_J$) for XO-3b. Clearly, there is considerable uncertainty in the value of the circularization time; however, because circumstellar disks appear to be lost after 10–20 Myr (e.g., Haisch et al. 2001; Mamajek et al. 2004), it appears that XO-3b perhaps should have circularized by now if it originally arrived at its current location while the circumstellar disk was still in place (i.e., through migration). If instead XO-3b has been scattered in to its current location (e.g., Ford & Rasio 2007) more recently, there may not have been enough time for circularization to occur, particularly for the parameters corresponding to the smaller radius for XO-3b. A third possibility is that additional, undetected planets orbiting XO-3 maintain the eccentricity of XO-3b (e.g., Adams & Laughlin 2006). It is interesting to note though that for planets in short period, eccentric orbits such as XO-3b, the tides raised in the planet can deposit substantial energy into the planet (e.g., Gu et al. 2003; Adams & Laughlin 2006) that can inflate it to radii corresponding to the larger value we measure (Gu et al. 2003). It therefore appears XO-3b can again serve as a very interesting benchmark for studies of tidal circularization and tidal heating once a more accurate radius can be established for the planet.

5. SUMMARY

XO-3b is a massive planet or low-mass brown dwarf in a short-period (3.2 day), eccentric ($e = 0.26$) orbit, around a somewhat evolved F5 star. There is relatively large uncertainty in the planetary parameters owing to the unknown distance to XO-3. The mass of XO-3b is 11.57–13.97 M_J, and the radius is 1.10–2.11 R_J. The larger mass and radius are favored by our spectroscopic analysis of XO-3, and the smaller values are favored by the light-curve analysis. A precise trigonometric parallax measurement or more accurate photometric light-curve data are needed to distinguish between these values.

We wish to thank the anonymous referee for many useful comments that improved the manuscript. The University of Hawaii staff have made the operation on Maui possible; we thank especially Bill Giebink, Les Hieda, Jake Kamibayashi, Jeff Kuhn, Haosheng Lin, Mike Maberry, Daniel O'Gara, Joey Perreira, Kaila Rhoden, and the director of the IFA, Rolf-Peter Kudritzki.

This research has made use of a Beowulf cluster constructed by Frank Summers; the SIMBAD database, operated at CDS, Strasbourg, France; data products from the Two Micron All Sky Survey (2MASS) and the Digitized Sky Survey (DSS); source code for transit light curves (Mandel & Agol 2002); and community access to the Hobby-Eberly Telescope (HET), which is a joint project of the University of Texas at Austin, the Pennsylvania State University, Stanford University, Ludwig-Maximilians-Universität München, and Georg-August-Universität Göttingen. The HET is named in honor of its principal benefactors, William P. Hobby and Robert E. Eberly. We thank the HET nighttime and daytime support staff. We also wish to thank the support staff at McDonald Observatory, and to especially thank M. Huerta for his assistance observing at the 2.7 m HJS Telescope.

XO is funded primarily by NASA Origins grant NNG06GG92G and the Director's Discretionary Fund of STScI. C. M. Johns-Krull and L. Prato wish to acknowledge partial support from NASA Origins of Solar Systems grant 05-SSO05-86. We thank Brian Skiff and Josh Winn for noting that a preprint had an error in the coordinates and there was a sign error in our radial velocity fitting algorithm, respectively; both were corrected prior to publication.

REFERENCES

Adams, F. C., & Laughlin, G. 2006, ApJ, 649, 1004
Allende Prieto, C., Asplund, M., López, R. J. G., & Lambert, D. L. 2002, ApJ, 567, 544
Aufdenberg, J. P., Ludwig, H.-G., & Kervella, P. 2005, ApJ, 633, 424
Bakos, G. Á., et al. 2007, ApJ, 670, 826
Baraffe, I., Chabrier, G., Barman, T. S., Allard, F., & Hauschildt, P. H. 2003, A&A, 402, 701
Bessell, M. S. 2000, PASP, 112, 961
Bessell, M. S., & Brett, J. M. 1988, PASP, 100, 1134
Bevington, P. R. & Robinson, D. K. 1992, Data Reduction and Error Analysis for the Physical Sciences (New York: McGraw Hill)
Bodenheimer, P., Hubickyj, O., & Lissauer, J. J. 2000, Icarus, 143, 2
Bodenheimer, P., Laughlin, G., & Lin, D. N. C. 2003, ApJ, 592, 555
Bodenheimer, P., Lin, D. N. C., & Mardling, R. A. 2001, ApJ, 548, 466
Boesgaard, A. M., Budge, K. G., & Ramsay, M. E. 1988, ApJ, 327, 389
Boss, A. P. 1997, Science, 276, 1836
———. 2000, ApJ, 536, L101
———. 2002, ApJ, 567, L149
Bouvier, J., et al. 2007, A&A, 463, 1017
Burke, C. J., et al. 2007, preprint (arXiv:0705.0003)
Burrows, A., Hubbard, W. B., Lunine, J. I., & Liebert, J. 2001, Rev. Mod. Phys., 73, 719
Butler, R. P., Marcy, G. W., Williams, E., Hauser, H., & Shirts, P. 1997, ApJ, 474, L115
Butler, R. P., Marcy, G. W., Williams, E., McCarthy, C., Dosanjh, P., & Vogt, S. S. 1996, PASP, 108, 500
Butler, R. P., Vogt, S. S., Marcy, G. W., Fischer, D. A., Wright, J. T., Henry, G. W., Laughlin, G., & Lissauer, J. J. 2004, ApJ, 617, 580
Claret, A. 2000, A&A, 363, 1081
Cochran, W. 2000, FTS Spectrum of I2 Cell HRS3 at 69.9 C. (Sunspot NSO), ftp://nsokp.nso.edu/FTS_cdrom/FTS50/001023R0.004
Cox, A. N. 2000, Allen's Astrophysical Quantities (4th ed.; New York: AIP Press)
Cumming, A., Marcy, G. W., & Butler, R. P. 1999, ApJ, 526, 890
Demarque, P., Woo, J.-H., Kim, Y.-C., & Yi, S. K. 2004, ApJS, 155, 667
Deming, D., Harrington, J., Laughlin, G., Seager, S., Navarro, S. B., Bowman, W. C., & Horning, K. 2007, ApJ, 667, L199
Eggenberger, A., Udry, S., & Mayor, M. 2004, A&A, 417, 353
Fischer, D. A., & Valenti, J. 2005, ApJ, 622, 1102
Ford, E. B., & Rasio, F. A. 2007, preprint (astro-ph/0703163)
Forrest, W. J., et al. 2004, ApJS, 154, 443
Fortney, J. J., Marley, M. S., & Barnes, J. W. 2007, ApJ, 659, 1661
Gonzalez, G. 1997, MNRAS, 285, 403
Gu, P.-G., Lin, D. N. C., & Bodenheimer, P. H. 2003, ApJ, 588, 509
Haisch, K. E., Jr., Lada, E. A., & Lada, C. J. 2001, ApJ, 553, L153
Halbwachs, J. L., Mayor, M., & Udry, S. 2005, A&A, 431, 1129
Hale, A. 1994, AJ, 107, 306
Hatzes, A. P., Cochran, W. D., & Johns-Krull, C. M. 1997, ApJ, 478, 374
Høg, E., et al. 2000, A&A, 355, L27
Hilditch, R. W. 2001, An Introduction to Close Binary Stars (Cambridge: Cambridge Univ. Press)
Hillenbrand, L. A., & White, R. J. 2004, ApJ, 604, 741
Hinkle, K. H., Joyce, R. R., Sharp, N., & Valenti, J. A. 2000, Proc. SPIE, 4008, 720
Hubickyj, O., Bodenheimer, P., & Lissauer, J. J. 2005, Icarus, 179, 415
Huerta, M. 2007, Ph.D. thesis, Rice Univ,
Huerta, M., Johns-Krull, C. M., Hartigan, P., Prato, L. A., & Jaffe, D. 2008, ApJ, in press (arXiv:0711.2505)
Inaba, S., Wetherill, G. W., & Ikoma, M. 2003, Icarus, 166, 46
Ivanov, P. B., & Papaloizou, J. C. B. 2007, MNRAS, 376, 682
Jones, H. R. A. 2004, in AIP Conf. Proc. 713, The Search for Other Worlds, ed. S. S. Holt & D. Deming (New York: AIP Press), 17
Landolt, A. U. 1992, AJ, 104, 340
Livio, M., & Pringle, J. E. 2003, MNRAS, 346, L42
Mamajek, E. E., Meyer, M. R., Hinz, P. M., Hoffmann, W. F., Cohen, M., & Hora, J. L. 2004, ApJ, 612, 496
Mandel, K., & Agol, E. 2002, ApJ, 580, L171
Mandushev, G., et al. 2005, ApJ, 621, 1061
———. 2007, preprint (arXiv:0708.0834)
Martínez Fiorenzano, A. F., Gratton, R. G., Desidera, S., Cosentino, R., & Endl, M. 2005, A&A, 442, 775
Mathieu, R. D. 1994, ARA&A, 32, 465
Mayer, L., Quinn, T., Wadsley, J., & Stadel, J. 2002, Science, 298, 1756
McCullough, P. R., & Burke, C. J. 2007, in ASP Conf. Ser. 366, Transiting Extrapolar Planets Workshop, ed. C. Alfonso, D. Weldrake, & Th. Henning (San Francisco: ASP), 70
McCullough, P. R., Stys, J. E., Valenti, J. A., Fleming, S. W., Janes, K. A., & Heasley, J. N. 2005, PASP, 117, 783
McCullough, P. R., et al. 2006, ApJ, 648, 1228
Murray, N., Hansen, B., Holman, M., & Tremaine, S. 1998, Science, 279, 69
Nelder, J. A., & Mead, R. 1965, Comput. J., 7, 308
Neuhäuser, R., Guenther, E. W., Wuchterl, G., Mugrauer, M., Bedalov, A., & Hauschildt, P. H. 2005, A&A, 435, L13
Nidever, D. L., Marcy, G. W., Butler, R. P., Fischer, D. A., & Vogt, S. S. 2002, ApJS, 141, 503
O'Donovan, F. T., et al. 2006a, ApJ, 644, 1237
———. 2006b, ApJ, 651, L61
Papaloizou, J. C. B., Nelson, R. P., Kley, W., Masset, F. S., & Artymowicz, P. 2007, in Protostars and Planets V, ed. B. Reipurth, D. Jewitt, & K. Keil (Tucson: Univ. Arizona Press), 655
Pollack, J. B., Hubickyj, O., Bodenheimer, P., Lissauer, J. J., Podolak, M., & Greenzweig, Y. 1996, Icarus, 124, 62
Queloz, D., Henry, G. W., Sivan, J. P., Baliunas, S. L., Beuzit, J. L., Donahue, R. A., Mayor, M., Naef, D., Perrier, C., & Udry, S. 2001, A&A, 379, 279
Ribas, I., & Miralda-Escudé, J. 2007, A&A, 464, 779
Santos, N. C., Israelian, G., & Mayor, M. 2003, in The Future of Cool-Star Astrophysics: 12th Cambridge Workshop on Cool Stars, Stellar Systems, and the Sun, ed. A. Brown, G. M. Harper, & T. R. Ayres (Boulder: Univ. Colorado), 148
———. 2004, A&A, 415, 1153
Santos, N. C., et al. 2002, A&A, 392, 215
Sato, B., et al. 2005, ApJ, 633, 465
Skrutskie, M. F. et al. 2006, AJ, 131, 1163
Sozzetti, A. 2004, MNRAS, 354, 1194
Sozzetti, A., Torres, G., Charbonneau, D., Latham, D. W., Holman, M. J., Winn, J. N., Laird, J. B., & O'Donovan, F. T. 2007, ApJ, 664, 1190
Sozzetti, A., et al. 2004, ApJ, 616, L167
Torres, G., Konacki, M., Sasselov, D. D., & Jha, S. 2004, ApJ, 609, 1071
Tull, R. G. 1998, Proc. SPIE, 3355, 387
Tull, R. G., MacQueen, P. J., Sneden, C., & Lambert, D. L. 1995, PASP, 107, 251
Udry, S., Fischer, D., & Queloz, D. 2007, in Protostars and Planets V, ed. B. Reipurth, D. Jewitt, & K. Keil (Tucson: Univ. Arizona Press), 685
Udry, S., Mayor, M., Naef, D., Pepe, F., Queloz, D., Santos, N. C., & Burnet, M. 2002, A&A, 390, 267
Udry, S., Mayor, M., & Santos, N. C. 2003, A&A, 407, 369
Valenti, J. A., & Fischer, D. A. 2005, ApJS, 159, 141 (VF05)
Valenti, J. A., & Piskunov, N. 1996, A&AS, 118, 595
VandenBerg, D. A., & Clem, J. L. 2003, AJ, 126, 778
Wallace, L., Hinkle, K., & Livingston, W. 1998, An Atlas of the Spectrum of the Solar Photosphere from 13,500 to 28,000 cm^{-1} (3570 to 7405 Å) (Tucson: NOAO)
Wu, Y. 2003, in ASP Conf. Ser. 294, Scientific Frontiers in Research on Extrasolar Planets, ed. D. Deming & S. Seager (San Francisco: ASP), 213
Zucker, S., & Mazeh, T. 2002, ApJ, 568, L113